Ultraslow serotonin oscillations in the hippocampus delineate substates across NREM and waking

Claire Cooper[1*] , Daniel Parthier[1], Jérémie Sibille[1], John Tukker[1,2], Nicolas X. Tritsch[3], Dietmar Schmitz[1,2,4,5,7*]

[1] Charité-Universitätsmedizin Berlin, corporate member of Freie Universität Berlin and Humboldt-Universität zu Berlin, Neuroscience Research Center, 10117 Berlin, Germany.

[2] German Center for Neurodegenerative Diseases (DZNE) Berlin, 10117 Berlin, Germany.

[3] Charité-Universitätsmedizin Berlin, corporate member of Freie Universität Berlin and Humboldt-Universität Berlin, Einstein Center for Neuroscience, 10117 Berlin, Germany.

[4] Charité-Universitätsmedizin Berlin, corporate member of Freie Universität Berlin and Humboldt-Universität Berlin, NeuroCure Cluster of Excellence, 10117 Berlin, Germany.

[5] Humboldt-Universität zu Berlin, Bernstein Center for Computational Neuroscience, Philippstr. 13, 10115 Berlin, Germany

[6] Neuroscience Institute, New York University Grossman School of Medicine, New York 10016, NY, USA.

*To whom correspondence should be addressed:

Email: dietmar.schmitz@charite.de, claire.cooper@charite.de

Competing Interest Statement: The authors declare no competing interest.

Keywords: Serotonin, oscillation, hippocampus, ripples, behavioral state

Abstract

Beyond the vast array of functional roles attributed to serotonin (5-HT) in the brain, changes in 5-HT levels have been shown to accompany changes in behavioral states, including WAKE, NREM and REM sleep. Whether 5-HT dynamics at shorter time scales can be seen to delineate substates within these larger brain states remains an open question. Here, we performed simultaneous recordings of extracellular 5-HT using a recently-developed G Protein–Coupled Receptor-Activation–Based 5-HT sensor (GRAB5-HT3.0) and local field potential (LFP) in the hippocampal CA1, which revealed the presence of prominent ultraslow (<0.05 Hz) 5-HT oscillations both during NREM and WAKE states. Interestingly, the phase of these ultraslow 5-HT oscillations was found to distinguish substates both within and across larger behavioral states. Hippocampal ripples occurred preferentially on the falling phase of ultraslow 5-HT oscillations during both NREM and WAKE, with higher power ripples concentrating near the peak specifically during NREM. By contrast, hippocampal-cortical coherence was strongest and microarousals and EMG peaks were most prevalent during the rising phase in both wake and NREM. Overall, ultraslow 5-HT oscillations delineate substates within the larger behavioral states of NREM and WAKE, thus potentially temporally segregating internal memory consolidation processes from arousal-related functions.

Main Text

Introduction

The impact of the outside world on neural activity is highly dynamic and dependent on the state of the brain. During waking behavior, sensory stimuli are actively processed by the brain and shape ongoing brain activity, whereas during sleep, the impact of such external stimuli is reduced in favor of internally-generated rhythms. Transition among behavioral states is accompanied by changes in the extracellular levels of neuromodulators. One such neuromodulator, serotonin (5-HT), shows clear state-dependent changes in activity, with the firing of 5-HT neurons in the brainstem being highest during waking, intermediate during NREM, and lowest during REM states (1, 2). Furthermore, changes in 5-HT levels have been causally linked to brain state changes, though some controversy over the direction of such changes remains. While some studies suggest a wake-promoting role for 5-HT, others propose that 5-HT increases sleep drive over the course of waking (3, 4). In either case, state-dependent changes in 5-HT levels can be seen to reorganize brain networks in response to ongoing functional demands.

Beyond traditional brain states, recent attention has been drawn to the existence of substates within these larger brain states. NREM sleep, for example, has been shown to contain periods of high and low arousal (5, 6). In these studies, high arousal substates were associated with higher heart rate and sensitivity to auditory stimuli, while low arousal substates contained more hippocampal ripples and sleep spindles. Therefore, substates in NREM may mediate the balance between processing external stimuli and carrying out internal brain processes, such as memory consolidation. Importantly, in both studies, these substates were delineated by the phase of ultra-slow oscillations (< 0.1 Hz) of sigma power and noradrenaline levels, respectively. While NREM substates have not yet been examined in relation to 5-HT levels, ultra-slow oscillations have been observed in population activity in the Dorsal Raphe Nucleus (DRN) (7, 8), as well as in extracellular 5-HT levels in the hippocampal dentate gyrus (9) during NREM, suggesting that 5-HT may also distinguish pro-arousal and pro-memory substates.

5-HT is a key modulator for many brain functions, which is reflected by the highly extensive projections of serotonergic fibers throughout the mammalian brain. Especially dense are the connections from the midbrain raphe nuclei, the source of 5-HT in the brain, to the hippocampus,

a region important for memory processing (10). Hallmarks of the hippocampus, ripples are transient fast oscillations (120-250 Hz) observed in the local field potential (LFP) and have been shown functionally to underlie memory consolidation and replay (11). While the contribution of 5-HT to memory processing remains unclear, with different studies supporting facilitating vs. suppressing roles (12-17), the three studies examining the effect of 5-HT modulation on ripples all found a suppressive effect (18-20). However, interpreting these studies is made difficult by the methods used to manipulate 5-HT levels, namely optogenetic activation of 5-HT neurons and pharmacologic interventions. Both methods involve simultaneous brain-wide increases of 5-HT levels, which has the potential to activate 5-HT sub-systems which are not naturally active together, such as the reward-activated and movement initiation-activated serotonergic fibers described in the dorsal hippocampus (21). Further rendering these studies hard to interpret is the question of physiologically plausible dose, as biphasic dose-dependent effects of 5-HT have been described (22).

To bypass such constraints, in the present study we utilized the recently-developed G Protein–Coupled Receptor-Activation–Based (GRAB) 5-HT sensor, which allows for the measurement of physiological changes in local extracellular 5-HT concentrations with high spatial and temporal resolution (23). Alongside 5-HT levels, we recorded hippocampal activity with silicon probes in order to examine potential correlations between local 5-HT fluctuations and behavioral states and substates in the dorsal CA1 in freely-moving mice. After simultaneous fiber photometry and LFP recordings, we could identify substates of NREM and WAKE delineated by different phases of ultraslow 5-HT oscillations. These substates roughly corresponded to periods of higher and lower arousal, with lower arousal associated with the preferential occurrence of ripples, and higher arousal with the occurrence of microarousals (MAs) as well as peaks in the EMG and hippocampal-cortical coherence.

Results

In order to simultaneously record local 5-HT levels and electrophysiological signals, we first injected mice with a virus encoding the GRAB5-HT3.0 sensor (AAV9-hSyn-5HT3.0) in the right dorsal CA1 (23). Simultaneous fiber photometry and electrophysiology recordings were achieved by implanting an optic fiber (400 µm) above the injection site (Figure 1A) and a silicon probe in the left dorsal CA1, at the same anterior-posterior coordinates as the site of viral injection (see Methods).

To verify that the sensor reports changes in local 5-HT levels, we treated a subset of mice (n=3) with fluoxetine (10 mg/kg), an SSRI known to acutely increase extracellular 5-HT levels in the dorsal hippocampus (24). Compared to saline, fluoxetine significantly elevated fluorescence recorded by fiber photometry, confirming the sensitivity of the GRAB-5HT3.0 sensor to endogenous levels of 5-HT in the hippocampus of mice (Figure 1I).

In order to examine the relationship between 5-HT signals and hippocampal activity across brain states, we simultaneously recorded hippocampal GRAB5-HT3.0 fluorescence and local field potentials (LFP) in the home cage during normal behavior, which included both waking and sleeping bouts. Twelve recording sessions were conducted using six mice (1-3 sessions per mouse), all of which were included in subsequent analysis and statistical testing. Automated sleep-scoring (25) was performed on the LFP data, showing the occurrence of different behavioral states, namely WAKE, non-REM sleep (NREM), REM sleep, and microarousals (MA), with different frequencies throughout the recording sessions (Figure 1G). Consistent with prior reports in the hippocampus (26), 5-HT levels were highest during WAKE, intermediate during NREM, and lowest during REM (Figure 1F.). During MAs, 5-HT levels were on average in between WAKE and NREM levels, but statistically indistinguishable from WAKE. Most strikingly,

we observed prominent ultraslow (<0.05 Hz.) oscillations of 5-HT levels during NREM (Figure 1D-E). These slow oscillations were reflected as a clear peak in the power spectrum at ~ 0.015 Hz (Figure 1H). A similar slow oscillation was also observed during WAKE, though with about half of the power of that seen in NREM.

Next, we sought to investigate whether substates could be defined relative to the phase of these slow 5-HT oscillations, as previously described for sigma power and noradrenaline oscillations (5, 6). The stronger ultraslow oscillations of 5-HT during NREM as compared to WAKE states led us to hypothesize a stronger coupling between ultraslow 5-HT oscillations and hippocampal activity during NREM than during WAKE.

5-HT and ripples

First, we looked at the relationship between ultraslow 5-HT oscillations and hippocampal ripples, the electrophysiological signature of memory consolidation. Given the noted shortcomings of the standard spectral filter-based methods for detecting ripples (27), and the recent surge of papers proposing alternative detection algorithms (28-32), we chose to detect ripples with a custom convolutional neural network (CNN) model (see Methods). 400 ms segments of eight LFP channels, including four cortical and four hippocampal channels, served as input to the model. After training and validation, the best-performing model consisted of four 2D convolutional blocks followed by two dense layers, outputting a 400-ms ripple probability vector (Figure 2A). This output vector was thresholded to detect ripples. Notably, the model was able to successfully distinguish ripples from non-ripple uniformly-propagating fast oscillations and movement-related noise (Figure 2B). Importantly, the features of detected events fell within the bounds expected for hippocampal ripples, with ripple duration and z-scored power showing a log-normal distribution (33) (Figure 2D).

In comparing ripple occurrence to the 5-HT signal, we noticed that both peaks of power in the ripple band (120-250 Hz.) (Figure 2E), a measure independent from ripple detection, and detected ripples (Figure 2F) tended to occur on the falling phase of slow 5-HT oscillations. In order to get a better sense of the timing between the 5-HT signal and ripple occurrence, we extracted ripple clusters, which were defined as groups of 10 or more ripples with an inter-ripple interval of three seconds or less (Figure 2G). These parameters were empirically observed to capture the clusters of ripples of various lengths occurring during the falling phase of 5-HT oscillations and to exclude the less numerous, non-clustered ripples occurring on the rising phase. Having defined ripple clusters, we were then able to isolate the first and last ripples of each cluster. When considering all ripples, before cluster extraction, the average ripple was seen to occur on the falling phase of the 5-HT oscillation, in both NREM and WAKE (Figure H1-2, first column). The first ripple of ripple clusters consistently occurred shortly after the peak in 5-HT in NREM, and at the peak in WAKE, while the last ripple occurred at the trough in both NREM and WAKE (Figure H1-2, columns 2-3). In summary, ripples were seen to span the length of the falling phase of slow 5-HT oscillations in both NREM and WAKE, though this relationship was generally stronger in NREM.

To further probe the relationship between ripple occurrence and 5-HT, we examined when ripples preferentially occur in relation to the phase of ultraslow 5-HT oscillations. We first looked at the distribution of inter-ripple intervals (IRIs) along different phases of ultraslow 5-HT oscillations measured in the 0.01 and 0.06 Hz frequency band (Figure 3A-C). There, consistent with what we observed in the cluster extraction data, we found lower IRIs along the falling phase (-180° : 0°), and higher IRIs along the rising phase (0° : 180°) (Figure 3B). These differences in IRIs between rising and falling phases were statistically significant for both NREM and WAKE after fitting a general linear mixed-model (GLMM) to the data, in which mouse and session were included as random effects (Figure 3C). As observed previously, the phase preference of NREM ripples was stronger than that of WAKE ripples, though both were prominent. Next, we calculated the 5-HT ultraslow phase preference of individual ripples during both NREM and WAKE (3E-F), where we again observed a clear falling phase preference in both states (Figure 3E1, 3E3). Remarkably,

the mean phase angles of NREM and WAKE ripples were very similar, at 101.1° and 99.6°, respectively, reflecting a very similar distribution of ripples along 5-HT ultraslow oscillations across states (Figure 3E3).

Finally, we wondered whether ripples of different strengths were preferentially distributed according to the phase of ultraslow 5-HT oscillations. To this end, we calculated the peak power for each detected ripple. Unlike what we previously observed with respect to ripple occurrence, the power of ripples in NREM showed a clear preference for the peak of ultraslow 5-HT oscillations, whereas no preference was observed in WAKE (Figure 3F.). We tested this trend by fitting a GLMM to the data, which rather than by 'rising phase 'vs. 'falling phase', was grouped this time by 'center '(-90° : 90°) vs. 'sides' (-180° : 90° and 90° : 180°), with mouse and session as random effects (Figure 3G). In summary, while ripples tend to show a preference for the falling phase of ultraslow 5-HT oscillations, stronger ripples tend to be statistically more likely near the peak of 5-HT in NREM, but not WAKE.

5-HT and microarousals

Given that ripples, the electrophysiological signature of memory consolidation, were shown to constitute one substate occurring during the falling phase of ultraslow 5-HT oscillations, we next looked for signs of arousal-associated substates, potentially occurring at different phases of the ultraslow 5-HT oscillation. To this end, we first considered the occurrence of MAs relative to 5-HT, given that MAs themselves constitute periods of heightened arousal within NREM (34, 25). MAs were observed together with peaks in the EMG during NREM, which appeared to be time-locked to 5-HT ultraslow oscillations (Figure 4A). On average, MAs occurred shortly before the peak of 5-HT on the rising phase (Figure 4D1-2). The same trend was observed when looking at the ultraslow 5-HT oscillation phase at which individual MAs occurred (Figure 4C), with the added information that MAs were generally much more likely on the rising phase than the falling phase. Therefore, not only do MAs themselves define periods of arousal within NREM, but their occurrence is biased by the phase of the ultraslow 5-HT oscillation, which designates periods when such arousals can occur.

5-HT and EMG

As MAs are only observed during NREM, we could not perform the same analysis on WAKE data. However, given that MAs are accompanied by peaks in the EMG, we next examined whether the EMG itself is time-locked to the phase of ultraslow 5-HT oscillations across states. Not surprisingly given the MA results, EMG peaks during NREM occurred preferentially during the rising phase of ultraslow 5-HT oscillations (Figure 4E,F, left). Interestingly, EMG peaks during WAKE were also observed preferentially in the rising phase (Figure 4E,F, right). After fitting a GLMM to the data, with random effects of mouse and session, the difference in EMG between the rising and falling phase was shown to be significant in both states, with the effect in NREM being stronger than that in WAKE (Figure 4G). Therefore, the rising phase of ultraslow 5-HT oscillations can be seen to constitute a substate of heightened arousal, both in terms of MA occurrence during NREM, and the EMG itself during both NREM and WAKE states.

5-HT and hippocampal-cortical coherence

Coherence is a measure of synchrony between two brain areas thought to underlie neural communication (35). Changes in coherence, including hippocampal-cortical coherence, have been found to track changes in arousal, both across and within brain states (36-38). We therefore examined hippocampal-cortical coherence in relation to the phase of ongoing ultraslow 5-HT oscillations (Figure 5A). After computing coherence between pairs of hippocampal and cortical channels in both NREM and WAKE, we observed that in certain frequency bands, coherence was higher in the rising phase of ultraslow 5-HT oscillations than in the falling phase, in both states (Figure 5B). In order to more closely examine this trend, we looked at coherence by ultraslow 5-HT oscillation phase for each frequency band individually (Figure 5C). After fitting a GLMM to the

data, with random effects for mouse and session, we found significant differences in coherence by ultraslow 5-HT phase in theta, slow gamma, fast gamma and high frequency oscillation bands, but not in the delta band both in NREM and WAKE (Figure 5D). Thus, inter-areal neural communication seems to be gated by the phase of ultraslow 5-HT oscillations, whereby during the rising phase, coherence is higher and such communication is favored.

Discussion

After simultaneous recordings of hippocampal 5-HT levels and LFP across behavioral states, we observed prominent ultraslow oscillations of 5-HT, which timed the occurrence of several electrophysiological read-outs. Specifically, we found that substates according to arousal level, similar to those described in NREM by previous studies (5, 6), were closely linked to the phase of 5-HT ultraslow oscillations. Hippocampal ripples occurred preferentially during the falling phase of 5-HT oscillations, whereby hippocampal-cortical coherence was strongest and microarousals and EMG peaks were most prevalent during the rising phase. Importantly, these 5-HT-defined substates were observed to coordinate local and global brain activity not only within NREM, but also during WAKE states.

The prominence of internally-driven ultraslow 5-HT oscillations during NREM explains why many studies focus on these rhythms during sleep. Potentially due to the requirement of WAKE to integrate external signals, ultraslow 5-HT oscillations appear less prominently in waking behavior. Nevertheless, our data shows that these ultraslow rhythms also play a role in WAKE, albeit to a lesser extent than in NREM. Indeed, studies have shown that the phase of ultraslow EEG oscillations during WAKE determines fluctuations in behavioral performance and arousal, thus segmenting WAKE into ultraslow oscillation-defined substates (39-41). In our study, including both NREM and WAKE periods allowed us to additionally show that the organization of activity by ultraslow oscillations of 5-HT was seen to operate according to the same principles in both states, namely by segregating high arousal activity from low arousal internal processing. Rather than a special feature of NREM, the ultraslow 5-HT oscillation appears to be a more fundamental rhythm structuring brain activity. Along these lines, a recent study reported ultraslow oscillations in the firing of medial entorhinal cortex (mEC) neurons which persisted throughout movement and immobility periods, substates of waking behavior (42).

In our data, we observed that the rising phase of ultraslow 5-HT oscillations was linked to arousal-associated brain activity. Specifically, long range coherence, which has been shown to correlate with arousal and behavioral performance (37, 43), was seen to peak in the rising phase of ultraslow 5-HT oscillations across a broad range of frequencies. In this way, 5-HT can be observed to gate communication between the cortex and hippocampus, reducing such communication during the ripple-associated falling phase. This gating could serve to reduce sensory input during ‘internal ’hippocampal memory processing, effectively decreasing potential interference that would disrupt memory consolidation (44, 45). While the mechanism of 5-HT’s effect on long-range neural synchrony is not yet clear, it has been shown that 5-HT can alter sensory gating dependent on communication between the thalamus and hippocampus (46). Furthermore, a recent study showed that type 2 dentate spikes (DS2s) in the hippocampus constitute substates of high arousal within immobility periods (47). During DS2s, greater brain-wide activation was observed than during ripples, which mirrors the higher inter-areal coherence and likely higher arousal we observed during the rising phase of ultraslow 5-HT oscillations compared to the falling phase, when ripples preferentially occurred. The role of arousal-associated axo-axonic cells in producing DS2s suggests that these inhibitory cells may be a good target to further examine changes in arousal relative to ultraslow 5-HT oscillations.

Microarousals constitute periods of heightened arousability within NREM which have been hypothesized to maintain a link between the sleeper and the outside world (48). Further, given

their known association with increased hippocampal-cortical synchrony (49), it is not surprising that they, as well as their associated EMG peaks, like coherence, show a preference for the rising phase of ultraslow 5-HT oscillations. In fact, arousal from NREM sleep was shown to be more likely during NREM microstates with higher inter-cortical coherence (36). More surprising was the finding that the EMG signal during WAKE is also locked in the same way to ultraslow 5-HT oscillations. Some studies have shown serotonergic control of movement in the hippocampus. Specifically, local infusion of 5-HT into the hippocampus was seen to induce locomotion and serotonergic fibers in CA1 have been shown to activate upon movement initiation (50, 21). Despite this link between 5-HT activity and locomotion in the hippocampus, it remains puzzling that the EMG signal, which reflects spontaneous and irregular movement, was observed in our data to be consistently coupled to the infraslow 5-HT oscillation. While the literature linking 5-HT and repetitive movements could shed more light on the question (51, 52), further studies examining the link between hippocampal 5-HT and movement are required to clarify this relationship.

According to studies performed to date, increasing 5-HT levels reduces ripple incidence (18-20). Based on these findings, one would expect a negative linear relationship in which ripples occur at the trough of 5-HT fluctuations, as was reported in the case of acetylcholine (53). In our study, however, the relationship between ripples and 5-HT levels was seen to be more complicated. The preference of ripples for the falling phase of ultraslow 5-HT oscillations within states shows that the dynamics of 5-HT change are more determining for ripple occurrence than the absolute 5-HT level, at this time scale. However, when looking at a longer time scale, namely across states, the relationship between 5-HT level and ripple incidence shows an inverted-U shape, with ripples occurring preferentially at the intermediate 5-HT levels observed in NREM (Figure 6).

Support for the importance of 5-HT release dynamics in consequent brain activity and behavioral outcomes comes from a study showing different behavioral consequences of burst versus tonic 5-HT release (54). Given their own findings that burst, but not tonic DRN stimulation induced waking, as well as studies showing that burst-firing of DRN neurons is associated with salient events (55-56), Oikonomou and colleagues posited that 5-HT released in bursts is arousing, whereas tonic release controls slow behavioral state changes, such as increasing sleep drive during wake behavior. Along these lines, the regular bursts of firing observed in a subset of DRN neurons at ultraslow frequencies *in vitro* (8), likely corresponding to the rising phase of ultraslow 5-HT oscillations in our data, could be seen to signal the regular arousing signals which we observe in our ultraslow 5-HT oscillation-defined substates. Ambient 5-HT levels arising from tonic state-dependent firing, on the other hand, could dictate the incidence range in which ripples can occur on a slower time-scale.

A potential mechanism for how different 5-HT release dynamics could differentially affect the hippocampal network at the synaptic level comes from a study on extrasynaptic 5-HT release (57). In this study, high frequency (10-20 Hz), but not low frequency (1 Hz) stimulation was shown to induce extrasynaptic release of 5-HT in the leech Retzius neuron (57). The effect of such extrasynaptic release would be the targeting of receptors and/or neurons not affected by exclusively synaptic release, thus changing the overall network response to 5-HT.

While ripple incidence was biased to the falling phase of ultraslow 5-HT oscillations, higher power ripples were found to cluster around the peak of ultraslow oscillations. It follows that, during NREM, the peak of 5-HT oscillations could define a heightened period of ripple propagation to the cortex, which has been shown to be greater in higher power ripples (58). As hippocampal-cortical interaction during ripples is thought to be a key factor in the consolidation of memory during NREM, the peak of ultraslow 5-HT oscillations could be seen to time memory consolidation itself (59, 60). Further studies are necessary to clarify the relationship between ultraslow 5-HT oscillations, ripple propagation and memory processes.

Both *in vivo* studies showing reduced ripple incidence after increasing 5-HT levels manipulated 5-HT levels systemically, either through intraperitoneal injections of an SSRI, or global activation of

Median Raphe Nucleus (MRN) neurons (18-20). Given the regional specificity of the 5-HT system, such systemic activation has the potential to introduce effects both non-specific to the region of interest, and potentially non-physiological. Systemic administration of a HTR4 agonist, for example, was shown to inhibit locomotion in an open field test, whereas local manipulation of CA1 terminals did not (14). Furthermore, different 5-HT fibers in CA1 were shown to be active during movement initiation and reward (21), indicating that even activating 5-HT fibers within one region at the same time has the potential to activate systems which are not naturally active together. Finally, the mode of systemic release has been shown to make a difference in the resulting behavioral outcome and neural response. In one study, phasic and chronic stimulation of the DRN were shown to inhibit and promote locomotion, respectively (61). In another study, DRN neurons were shown to have both immediate, *i.e.* phasic, responses to reward and punishment, but also adjust their tonic firing on the time scale of minutes (55).

The conclusion of the three prior studies showing reduced ripples with increased 5-HT can further be understood in terms of physiological dose. Inhibitory HTR1a receptors have been shown to be expressed extrasynaptically in CA1 pyramids (62). Therefore, one could imagine that after *in vitro* bath application of 5-HT, or excess stimulation of 5-HT terminals, leading to extrasynaptic release and/or volume transmission of 5-HT, these receptors could be selectively engaged to silence pyramids and shut-down the network. In fact, an inverted-U dose response curve with suppression at higher doses, similar to that found between 5-HT levels and ripples across states, was observed in a computational study of the effect of 5-HT on spatial working memory in the medial prefrontal cortex (63).

These methodological considerations highlight the benefit of the correlative approach adopted here, measuring local 5-HT levels and brain activity simultaneously. While causal relationships cannot be determined from this strategy, the relationship observed between 5-HT levels and ripples can be used to inform future causal studies in a data-driven way. For example, the findings highlight the importance of having a detailed look at the relationship between different 5-HT release dynamics and hippocampal cell and network responses. Furthermore, modulating the frequency or strength of the slow 5-HT oscillations, as done in (6) for spindle oscillations and noradrenaline, could provide insight into how 5-HT tone and phasic release modulate ripples in a realistic setting.

Materials and Methods

Animals

All experimental procedures were performed following the Guide for Animal Care and Use of Laboratory Animals. Male C57BL6/J mice (Jackson Laboratory) between 2-6 months of age were used for experiments. The mice were housed in groups of 2-5 animals prior to surgery, and singly after surgery, in a reverse 12/12 hour light-dark cycle (lights on 10 p.m. to 10 a.m.) with ad libitum access to food and water.

Surgery

For viral injection, as well as for the implantation of optic fiber cannulae and silicon probes, mice were anesthetized with isoflurane (4%) and placed in a stereotactic frame (Kopf Instruments). Body temperature was maintained at 38° C by a heating pad (Harvard Instruments). The isoflurane level was slowly reduced to 1-2 % to maintain anesthesia throughout the surgery. Mice were injected with ketoprofen (10 mg/kg, s.c.). Hair was removed with a depilatory cream, the scalp was cleaned with ethanol and iodine solutions, and the skull exposed.

Viral Injection and Optic Fiber Implantation

A craniotomy was performed by driling a small hole above the right dorsal CA1 (AP -2.3 mm, ML -2.00 mm). A glass injection micropipette with a 100 µm tip was pulled, filled with mineral oil, and connected to a Hamilton syringe attached to a microsyringe pump (KD Scientific, Legato 111).

250 nl of AAV9-hSyn-5HT3.0 (WZ Biosciences) was injected at a rate of 100 nl/min and a depth of 1.3 mm below the dura. After injection, the pipette was left in place for 5 minutes before slowly bringing it up out of the brain over the course of 20-30 minutes. Saline was administered to the craniotomy site to keep the tissue moist throughout the procedure.
An optic fiber (Thorlabs CFML15L05) was then implanted above the injection site. Only fibers with >80 % transmission efficacy were used. The optic fiber was secured with C&B Metabond (Parkell). Dental cement was applied to exposed areas of the skull. Mice were kept in their home cages for 3 weeks to allow recovery from surgery and expression of the virus.

Silicon Probe Implantation and Electrophysiological Recordings
Three weeks after viral injection and optic fiber implantation, a second surgery was performed to implant a silicon probe (NeuroNexus, 64-channel, edge, 1 or 4 shanks), mounted onto a microdrive (NeuroNexus, dDrive) into the left dorsal CA1. To this end, anesthesia was induced, as previously described, and a mouse cap with copper mesh (3DNeuro) was cemented to the skull. A second craniotomy was then performed over the right dorsal CA1 (AP -2.3 mm, ML +2.00 mm). The probe was slowly lowered and secured with C&B Metabond at a depth of 0.8 mm below the dura. The exposed brain was covered with a mixture of heated bone wax and mineral oil. A grounding screw was placed over the cerebellum and soldered to the ground electrode on the probe and the mouse cap. The mouse was allowed to recover for five days, at which point the probe was further lowered until the prominent spikes and sharp wave ripples characteristic of the CA1 pyramidal layer were observed. Data was recorded with an Open Ephys system at 20 kHz.

Fiber photometry
Fiber photometry was performed as described in (67). Briefly, a fiber-coupled 470 nm LED (Thorlabs) was used to send excitation light in continuous wave mode through a fiber optic patch cord (Doric) to the mouse's optic fiber implant via a fluorescence mini-cube (Doric). Emitted light traveled back through the same optic fiber patch cord to the mini-cube, and was collected by a photoreceiver (Newport, DC mode). Signal collected by the photoreceiver was digitized at 5 kHz with a National Instruments acquisition board (NI BNC-2090A) and analyzed using Wavesurfer (Janelia).
Preprocessing of fiber photometry data was performed as described by Thomas Akam (Github, Thomas Akam, photometry_preprocessing: https://github.com/ThomasAkam/photometry_preprocessing/tree/master. Namely, raw fiber photometry data was first downsampled to 1250 Hz for comparison with electrophysiology data, and low pass filtered at 20 Hz. using MATLAB's (R2021a) lowpass function. Next slow drift in signal due to photobleaching was corrected by fitting a second-order exponential function. Finally, in order to compare photometry data across sessions and mice, the signals were z-scored.

Fluoxetine injections
In order to show that the GRAB5-HT3.0 sensor used is responsive to changes in local 5-HT levels, 10 mg/kg fluoxetine-hydrochloride (Sigma-Aldrich) dissolved in saline or saline only (control) was administered intraperitoneally after a 20 min. baseline.

Dual fiber photometry and silicon probe recordings
Contralateral simultaneous recordings were chosen over ipsilateral due to the size of the optic fibers and fragility of the silicon probes, which prevented their implantation in close proximity. In addition to its adoption in a recent dual-recording study (65), this contralateral recording scheme can be justified due to the simultaneous occurrence of ripples, a major electrophysiological read-out in the current study, across hemispheres (66, 67), bilateral synchrony of ultraslow EEG oscillations (68), as well as the bilateral symmetry of the 5-HT system (69).
Fiber photometry and electrophysiological data were simultaneously recorded from double-implanted mice in their home cages for 2-3 hour sessions, containing both wake and sleep periods. Synchronization of photometry and electrophysiological data was performed by triggering recording onset with an Arduino pulse.

CNN for ripple detection

The custom CNN model used for ripple detection was inspired by the approach of (30) and can be found on GitHub (70). In their work, ripple detection was reframed from 1D thresholding of spectral features over time, to an image recognition problem, where the image consists of segments of LFP data from multiple channels containing ripples. Detection thus takes into account the classic laminar pattern of ripples, which is useful for distinguishing them from other fast oscillations or noise. Furthermore, this approach is unbiased in the sense that it doesn't rely upon a strict limitation of ripple features and, furthermore, has been shown to perform more consistently with data from different experimental sessions than standard filter-based detection (32).

Data preparation: In constructing our model, which is structurally simpler than that proposed in (30), we added cortical channels to the model input, which were helpful in excluding propagating noise and movement artifacts. Inputs to the network were prepared as follows: 4 neighboring channels in CA1 showing ripples were chosen. With 50 µm spacing between electrode sites, 4 channels showing ripple oscillations displayed characteristic amplitude changes that were key to distinguishing them from movement artifacts, fast gamma oscillations or other false positives often detected as ripples by traditional ripple detection algorithms. Additionally, four channels were chosen from the neocortex to increase the network's ability to rule out movement artifacts or other noise which propagates uniformly across channels. Data from the 8 channels was then z-scored and segmented into 400 ms chunks and these 8 channel x 400 ms chunks were fed in as 2D inputs to the network.

Ripple Annotation and Training Data: To prepare a training set, ripple start and stop times were labeled for 5,000 ripples occurring in data from three different mice. A key criterion for distinguishing ripples from non-ripples was signal modulation across hippocampal and cortical channels. Fast and transient oscillations in which the amplitude varied according to location relative to the center of the CA1 pyramidal layer were considered ripples, whereas oscillations in which the amplitude appeared constant across hippocampal or hippocampal and cortical channels were excluded. 400 ms data segments centered around the labeled ripples were extracted for the 8 input channels (4 hippocampal and 4 cortical). A label trace (1 x 400 ms) was generated for each segment in which time outside of ripples was taken to be 0, and time during ripples, 1. For training, 5,000 negative examples, i.e. data segments including no ripples, were also included. The timing of these segments were chosen at random such that there was no overlap between them and the ripple-containing segments, and were taken from the same 8 channels and three mice used for ripple-containing segments. Label traces were generated for each negative example consisting of a 1 x 400 ms trace of zeroes. Training data was split into a training set (80%) and a testing set (20%).

CNN Architecture: A custom convolutional neural network (CNN) was built using Python 3.9.12 and the following key python packages:
tensorflow 2.9.1
keras 2.9.0
numpy 1.23.0
scipy 1.8.1
The model was built within a custom model class called RipNet. RipNet consisted of four convolution blocks, with each block consisting of a 2D convolutional layer (Conv2D), followed by a Rectified Linear Unit (ReLU) activation layer and a Batch Normalization layer. Stride length was (2,2) for all blocks and kernel size was (1,1) for the first block, and (3,3) for the subsequent three blocks. The convolution blocks were followed by a Dropout layer (0.25), a Dense layer, a Batch Normalization layer, and a second Dropout layer (0.4). A sigmoid activation function on the final Dense layer provided the prediction trace, which gave the likelihood of ripple occurring as a number between 0 and 1, for the input trace provided. Ripples were detected when the prediction trace exceeded an empirically-determined threshold of 0.2. Ripple peak times were determined by taking the peak of the envelope of the ripple-band (120-250 Hz.) bandpass-filtered signal. Network architectures, i.e. the number of convolutional blocks, and hyperparameters, including the optimizer, learning rate and regularization, were tuned during training. After training, the best-

performing model consisted of four convolutional blocks, an Adam optimizer with a learning rate of 1e-4 and a decay rate of 1e-4/epochs, as well as L2 regularization (0.001) to prevent overfitting. Mean-squared error (MSE) was used as a loss function to compare the predicted trace to the ground truth trace.

Model performance: Model performance was evaluated based on ripples detected in two hours of data across two mice, which was not included in the training dataset. In this testing set, ripples were annotated manually and compared to model predictions. True positives (TPs) occurred when manually labeled ripples were also predicted by the model. False negatives (FNs) were marked where ripples were annotated, but not predicted by the model. False positives (FPs) encompassed ripples predicted by the model and not labeled manually, and upon second inspection, not considered ripples. Based on these metrics, the F1 value, which represents the harmonic mean of precision (TP / TP + FP) and recall (TP / TP + FN), was calculated as a measure of model performance. The F1 value was found to be 81.5% for the testing data set. Of note, this F1 value is higher than that reported for both the standard Butterworth filter method at optimized performance and the aforementioned previously published CNN (30), with F1 values of 68% and 65%, respectively.

State scoring

Behavioral states were designated as WAKE, NREM, REM or MA according to output of the SleepScoreMaster function from the Buzsaki lab code repository (https://github.com/buzsakilab/buzcode). The methodology for SleepScoreMaster's sleep score detection is described in (25). Briefly, the LFP power at low frequencies (< 25 Hz) was first used to distinguish NREM from 'other 'states. Next, the 'other 'states were assigned labels according to the narrow theta-band ratio (5-10 Hz / 2-6 Hz) and the EMG, with high theta ratio and low EMG corresponding to REM states, and remaining states being classified as WAKE (>40 s) or MA (<40 s). Detected states were then reviewed manually by the experimenter.

LFP Analysis

LFP analysis was performed using custom MATLAB code. Time-frequency power spectra were generated using the Stockwell Transform (71) with MATLAB's st function. Time-frequency power spectra were normalized to 0-1 for visualization. Phase angles were calculated using the Hilbert transform of the bandpass-filtered signal (0.01-0.06 Hz). Magnitude-squared wavelet coherence was calculated using MATLAB's wwcoherence function.

Histology

Transcardiac perfusion was performed after deep anesthesia with isoflurane with 4% paraformaldehyde (PFA) in 0.1 M sodium phosphate buffer. Brains were kept in PFA overnight, then sliced into 100 µM coronal sections with a vibratome (Leica). Slices were mounted using Fluoroshield with DAPI (Sigma) and endogenous fluorescence from the GRAB5-HT3.0 sensor was imaged with an Olympus VS120 slide scanning microscope. From these images, the expression of the GRAB5-HT3.0 sensor in the dorsal CA1 was verified.

Statistics

All plots with error bars or bounded lines reflect the mean across sessions +/- standard error of the mean. Statistics were performed in RStudio, using R version 4.3.2. As the data for all experiments is hierarchical, it is necessary to account for inter-mouse and inter-session variation (72). To this end, we fit general linear mixed models (GLMMs), including random effects terms for mouse and session ID. For Figure 1F, the *blme* package was used with a gaussian link function (73). For Figure 3, a gamma link function was used with the *glmmTMB* package (74). For Figures 4-5, a beta distribution link function was used with the *glmmTMB* package. *Emmeans* was used for post-hoc testing of fitted models (75) as well as a Bonferroni adjustment for multiple comparisons. For Figure 1I, a Wilcoxon ranked-sum test was used on the mean 5-HT levels in

584 fluoxetine and saline-injected mice in the 20 minutes period starting 20 minutes after the
585 injection.
586

587 **Acknowledgments**

588 We would like to acknowledge the Buzsàki lab for providing the virus expressing the GRAB5-
589 HT3.0 sensor we used in this study. We would also like to thank members of the Tritsch lab for
590 providing assistance with fiber photometry, especially James Taniguchi and Tony Garcia.

591

592 **Funding**

593 This study was supported by the German Research Foundation (Deutsche
594 Forschungsgemeinschaft (DFG), project 184695641 – SFB 958, project 327654276 – SFB 1315,
595 project 415914819 – FOR 3004, project 431572356, and under Germany's Excellence Strategy –
596 Exc-2049-390688087), by the Federal Ministry of Education and Research (BMBF, SmartAge-
597 project 01GQ1420B) and by the European Research Council (ERC) under the Europeans Union's
598 Horizon 2020 research and innovation program (grant agreement No. 810580).

599

600 **Author Contributions**

601 Conception and design: C.C., D.S.
602 Acquisition of data: C.C.
603 Analysis and interpretation of data: C.C., D.P.
604 Drafting or revising the article: C.C., D.S.
605 Contributed to new analytic tools or reagents: D.P., J.S., J.T., N.T.
606

607 **Data availability**

608 Data required to reproduce findings can be found on FigShare:
609 https://figshare.com/account/home#/projects/204408.

610

611 **References**

612

613 1. D. J. McGinty, R. M. Harper, Dorsal raphe neurons: depression of firing during sleep in cats.
614 *Brain Research* **101**, 569–575 (1976).
615 2. M. E. Trulson, B. L. Jacobs, Raphe unit activity in freely moving cats: correlation with level of
616 behavioral arousal. *Brain Res* **163**, 135–150 (1979).
617 3. R. Ursin, "Changing concepts on the role of serotonin in the regulation of sleep and waking"
618 in *Serotonin and Sleep: Molecular, Functional and Clinical Aspects*, J. M. Monti, S. R. Pandi-
619 Perumal, B. L. Jacobs, D. J. Nutt, Eds. (Birkhäuser, 2008), pp. 3–21.1.
620 4. J. M. Monti, S. R. Pandi-Perumal, B. L. Jacobs, D. J. Nutt, Serotonin and Sleep: Molecular,
621 Functional and Clinical Aspects (Springer Science & Business Media, 2008).
622 5. S. Lecci, *et al.*, Coordinated infraslow neural and cardiac oscillations mark fragility and offline
623 periods in mammalian sleep. *Sci Adv* **3**, e1602026 (2017).
624 6. A. Osorio-Forero, *et al.*, Noradrenergic circuit control of non-REM sleep substates. *Current*
625 *Biology* **31**, 5009-5023.e7 (2021).

7. T. Kato, *et al.*, Oscillatory Population-Level Activity of Dorsal Raphe Serotonergic Neurons Is Inscribed in Sleep Structure. *J. Neurosci.* **42**, 7244–7255 (2022).
8. B. Mlinar, A. Montalbano, L. Piszczek, C. Gross, R. Corradetti, Firing Properties of Genetically Identified Dorsal Raphe Serotonergic Neurons in Brain Slices. *Front Cell Neurosci* **10**, 195 (2016).
9. G. F. Turi, *et al.*, Modulation of infraslow oscillation in the dentate gyrus during Non-REM sleep. [Preprint] (2023). Available at: https://www.biorxiv.org/content/10.1101/2023.05.12.540575v1 [Accessed 30 April 2024].
10. B. L. Jacobs, E. C. Azmitia, Structure and function of the brain serotonin system. *Physiol Rev* **72**, 165–229 (1992).
11. G. Buzsáki, Hippocampal sharp wave-ripple: A cognitive biomarker for episodic memory and planning. *Hippocampus* **25**, 1073–1188 (2015).
12. A. Meneses, Serotonin, neural markers, and memory. *Front. Pharmacol.* **6** (2015).
13. R. Coray, B. B. Quednow, The role of serotonin in declarative memory: A systematic review of animal and human research. *Neurosci Biobehav Rev* **139**, 104729 (2022).
14. C. M. Teixeira, *et al.*, Hippocampal 5-HT Input Regulates Memory Formation and Schaffer Collateral Excitation. *Neuron* **98**, 992-1004.e4 (2018).
15. G. Zhang, *et al.*, Stimulation of serotonin 2A receptors facilitates consolidation and extinction of fear memory in C57BL/6J mice. *Neuropharmacology* **64**, 403–413 (2013).
16. G. Zhang, R. W. Stackman, The role of serotonin 5-HT2A receptors in memory and cognition. *Front. Pharmacol.* **6** (2015).
17. G. Zhang, *et al.*, Examination of the hippocampal contribution to serotonin 5-HT2A receptor-mediated facilitation of object memory in C57BL/6J mice. *Neuropharmacology* **109**, 332–340 (2016).
18. D. V. Wang, *et al.*, Mesopontine median raphe regulates hippocampal ripple oscillation and memory consolidation. *Nat Neurosci* **18**, 728–735 (2015).
19. R. ul Haq, *et al.*, Serotonin dependent masking of hippocampal sharp wave ripples. *Neuropharmacology* **101**, 188–203 (2016).
20. H. Shiozaki, N. Kuga, T. Kayama, Y. Ikegaya, T. Sasaki, Selective serotonin reuptake inhibitors suppress sharp wave ripples in the ventral hippocampus. *J Pharmacol Sci* **152**, 136–143 (2023).
21. A. Luchetti, *et al.*, Two Functionally Distinct Serotonergic Projections into Hippocampus. *J Neurosci* **40**, 4936–4944 (2020).
22. E. J. Calabrese, 5-Hydroxytryptamine (serotonin): biphasic dose responses. *Crit Rev Toxicol* **31**, 553–561 (2001).
23. J. Wan, *et al.*, A genetically encoded sensor for measuring serotonin dynamics. *Nat Neurosci* **24**, 746–752 (2021).
24. Y. Imoto, *et al.*, Role of the 5-HT4 receptor in chronic fluoxetine treatment-induced neurogenic activity and granule cell dematuration in the dentate gyrus. *Mol Brain* **8**, 29 (2015).
25. B. O. Watson, D. Levenstein, J. P. Greene, J. N. Gelinas, G. Buzsáki, Network homeostasis and state dynamics of neocortical sleep. *Neuron* **90**, 839–852 (2016).
26. S. P. Park, *et al.*, In vivo microdialysis measures of extracellular serotonin in the rat hippocampus during sleep-wakefulness. *Brain Res* **833**, 291–296 (1999).
27. A. A. Liu, *et al.*, A consensus statement on detection of hippocampal sharp wave ripples and differentiation from other fast oscillations. *Nat Commun* **13**, 6000 (2022).
28. Y. Watanabe, M. Okada, Y. Ikegaya, Towards threshold invariance in defining hippocampal ripples. *J. Neural Eng.* **18**, 066012 (2021).
29. E. Hagen, *et al.*, RippleNet: a Recurrent Neural Network for Sharp Wave Ripple (SPW-R) Detection. *Neuroinformatics* **19**, 493–514 (2021).
30. A. Navas-Olive, R. Amaducci, M.-T. Jurado-Parras, E. R. Sebastian, L. M. de la Prida, Deep learning-based feature extraction for prediction and interpretation of sharp-wave ripples in the rodent hippocampus. *eLife* **11**, e77772 (2022).
31. E. R. Sebastian, *et al.*, Topological analysis of sharp-wave ripple waveforms reveals input mechanisms behind feature variations. *Nat Neurosci* **26**, 2171–2181 (2023).

32. A. Navas-Olive, A. Rubio, S. Abbaspoor, K. L. Hoffman, L. M. de la Prida, A machine learning toolbox for the analysis of sharp-wave ripples reveals common waveform features across species. *Commun Biol* **7**, 1–15 (2024).
33. D. Levenstein, G. Buzsáki, J. Rinzel, NREM sleep in the rodent neocortex and hippocampus reflects excitable dynamics. *Nat Commun* **10**, 2478 (2019).
34. P. Halász, Hierarchy of micro-arousals and the microstructure of sleep. *Neurophysiologie Clinique/Clinical Neurophysiology* **28**, 461–475 (1998).
35. P. Fries, A mechanism for cognitive dynamics: neuronal communication through neuronal coherence. *Trends in Cognitive Sciences* **9**, 474–480 (2005).
36. H. Bastuji, A. Cadic-Melchior, M. Magnin, L. Garcia-Larrea, Intracortical Functional Connectivity Predicts Arousal to Noxious Stimuli during Sleep in Humans. *J Neurosci* **41**, 5115–5123 (2021).
37. L. M. F. Klaver, *et al.*, Spontaneous variations in arousal modulate subsequent visual processing and local field potential dynamics in the ferret during quiet wakefulness. *Cerebral Cortex* **33**, 7564–7581 (2023).
38. J. L. Cantero, M. Atienza, J. R. Madsen, R. Stickgold, Gamma EEG dynamics in neocortex and hippocampus during human wakefulness and sleep. *NeuroImage* **22**, 1271–1280 (2004).
39. M. D. Fox, A. Z. Snyder, J. L. Vincent, M. E. Raichle, Intrinsic Fluctuations within Cortical Systems Account for Intertrial Variability in Human Behavior. *Neuron* **56**, 171–184 (2007).
40. S. Monto, S. Palva, J. Voipio, J. M. Palva, Very Slow EEG Fluctuations Predict the Dynamics of Stimulus Detection and Oscillation Amplitudes in Humans. *J Neurosci* **28**, 8268–8272 (2008).
41. D. Sihn, S.-P. Kim, Brain Infraslow Activity Correlates With Arousal Levels. *Front. Neurosci.* **16** (2022).
42. S. Gonzalo Cogno, *et al.*, Minute-scale oscillatory sequences in medial entorhinal cortex. *Nature* **625**, 338–344 (2024).
43. M. Parto-Dezfouli, J. Vezoli, C. A. Bosman, P. Fries, Enhanced behavioral performance through interareal gamma and beta synchronization. *Cell Reports* **42**, 113249 (2023).
44. N. K. Logothetis, *et al.*, Hippocampal-cortical interaction during periods of subcortical silence. *Nature* **491**, 547–553 (2012).
45. M. Yang, N. K. Logothetis, O. Eschenko, Occurrence of Hippocampal Ripples is Associated with Activity Suppression in the Mediodorsal Thalamic Nucleus. *J Neurosci* **39**, 434–444 (2019).
46. J. Lee, S. Thwaites, A. Gogos, M. van den Buuse, Pharmacological Mechanisms Involved in Sensory Gating Disruption Induced by (±)-3,4-Methylene- Dioxymethamphetamine (MDMA): Relevance to Schizophrenia. *Brain Sci* **10**, 44 (2020).
47. J. S. Farrell, E. Hwaun, B. Dudok, I. Soltesz, Neural and behavioural state switching during hippocampal dentate spikes. *Nature* 1–6 (2024). https://doi.org/10.1038/s41586-024-07192-8.
48. P. Halász, M. Terzano, L. Parrino, R. Bódizs, The nature of arousal in sleep. *Journal of Sleep Research* **13**, 1–23 (2004).
49. G. Z. dos Santos Lima, *et al.*, Hippocampal and cortical communication around micro-arousals in slow-wave sleep. *Sci Rep* **9**, 5876 (2019).
50. H. Takahashi, Y. Takada, N. Nagai, T. Urano, A. Takada, Serotonergic neurons projecting to hippocampus activate locomotion. *Brain Research* **869**, 194–202 (2000).
51. B. D. Alvarez, C. Cavazos, C. A. Morales, S. M. Lopez, D. A. Amodeo, Impact of specific serotonin receptor modulation on restricted repetitive behaviors. *Frontiers in Behavioral Neuroscience* **16** (2022).
52. B. L. Jacobs, C. A. Fornal, Activity of brain serotonergic neurons in the behaving animal. *Pharmacol Rev* **43**, 563–578 (1991).
53. Y. Zhang, *et al.*, Cholinergic suppression of hippocampal sharp-wave ripples impairs working memory. *Proc. Natl. Acad. Sci. U.S.A.* **118**, e2016432118 (2021).
54. G. Oikonomou, *et al.*, The Serotonergic Raphe Promote Sleep in Zebrafish and Mice. *Neuron* **103**, 686-701.e8 (2019).
55. J. Y. Cohen, M. W. Amoroso, N. Uchida, Serotonergic neurons signal reward and punishment on multiple timescales. *eLife* **4**, e06346 (2015).

56. G. E. Paquelet, *et al.*, Single-cell activity and network properties of dorsal raphe nucleus serotonin neurons during emotionally salient behaviors. *Neuron* **110**, 2664-2679.e8 (2022).
57. C. Trueta, F. F. De-Miguel, Extrasynaptic exocytosis and its mechanisms: a source of molecules mediating volume transmission in the nervous system. *Front Physiol* **3**, 319 (2012).
58. N. Nitzan, *et al.*, Propagation of hippocampal ripples to the neocortex by way of a subiculum-retrosplenial pathway. *Nat Commun* **11**, 1947 (2020).
59. G. Rothschild, E. Eban, L. M. Frank, A cortical–hippocampal–cortical loop of information processing during memory consolidation. *Nat Neurosci* **20**, 251–259 (2017).
60. N. Maingret, G. Girardeau, R. Todorova, M. Goutierre, M. Zugaro, Hippocampo-cortical coupling mediates memory consolidation during sleep. *Nat Neurosci* **19**, 959–964 (2016).
61. P. A. Correia, *et al.*, Transient inhibition and long-term facilitation of locomotion by phasic optogenetic activation of serotonin neurons. *Elife* **6**, e20975 (2017).
62. M. Riad, *et al.*, Somatodendritic localization of 5-HT1A and preterminal axonal localization of 5-HT1B serotonin receptors in adult rat brain. *Journal of Comparative Neurology* **417**, 181–194 (2000).
63. M. Cano-Colino, R. Almeida, D. Gomez-Cabrero, F. Artigas, A. Compte, Serotonin Regulates Performance Nonmonotonically in a Spatial Working Memory Network. *Cerebral Cortex* **24**, 2449–2463 (2014).
64. A. C. Krok, *et al.*, Intrinsic dopamine and acetylcholine dynamics in the striatum of mice. *Nature* **621**, 543–549 (2023).
65. Y. Zhang, *et al.*, Interaction of acetylcholine and oxytocin neuromodulation in the hippocampus. *Neuron* (2024). https://doi.org/10.1016/j.neuron.2024.02.021.
66. J. J. Chrobak, G. Buzsáki, High-frequency oscillations in the output networks of the hippocampal-entorhinal axis of the freely behaving rat. *J Neurosci* **16**, 3056–3066 (1996).
67. G. Buzsáki, *et al.*, Hippocampal network patterns of activity in the mouse. *Neuroscience* **116**, 201–211 (2003).
68. Z. Liu, M. Fukunaga, J. A. de Zwart, J. H. Duyn, Large-Scale Spontaneous Fluctuations and Correlations in Brain Electrical Activity Observed with Magnetoencephalography. *Neuroimage* **51**, 102–111 (2010).
69. J. Ren, *et al.*, Anatomically Defined and Functionally Distinct Dorsal Raphe Serotonin Sub-systems. *Cell* **175**, 472-487.e20 (2018).
70. C. Cooper, ripNet. Github. https://github.com/clairecooper2193/ripNet Deposited 7 May 2024.
71. R. G. Stockwell, L. Mansinha, R. P. Lowe, Localization of the complex spectrum: the S transform. *IEEE Transactions on Signal Processing* **44**, 998–1001 (1996).
72. Z. Yu, *et al.*, Beyond t test and ANOVA: applications of mixed-effects models for more rigorous statistical analysis in neuroscience research. *Neuron* **110**, 21–35 (2022).
73. Y. Chung, S. Rabe-Hesketh, V. Dorie, A. Gelman, J. Liu, A Nondegenerate Penalized Likelihood Estimator for Variance Parameters in Multilevel Models. *Psychometrika* **78**, 685–709 (2013).
74. M. Brooks E., *et al.*, glmmTMB Balances Speed and Flexibility Among Packages for Zero-inflated Generalized Linear Mixed Modeling. *The R Journal* **9**, 378 (2017).
75. Lenth R (2024). _emmeans: Estimated Marginal Means, aka Least-Squares Means_. R package version 1.10.0, <https://CRAN.R-project.org/package=emmean

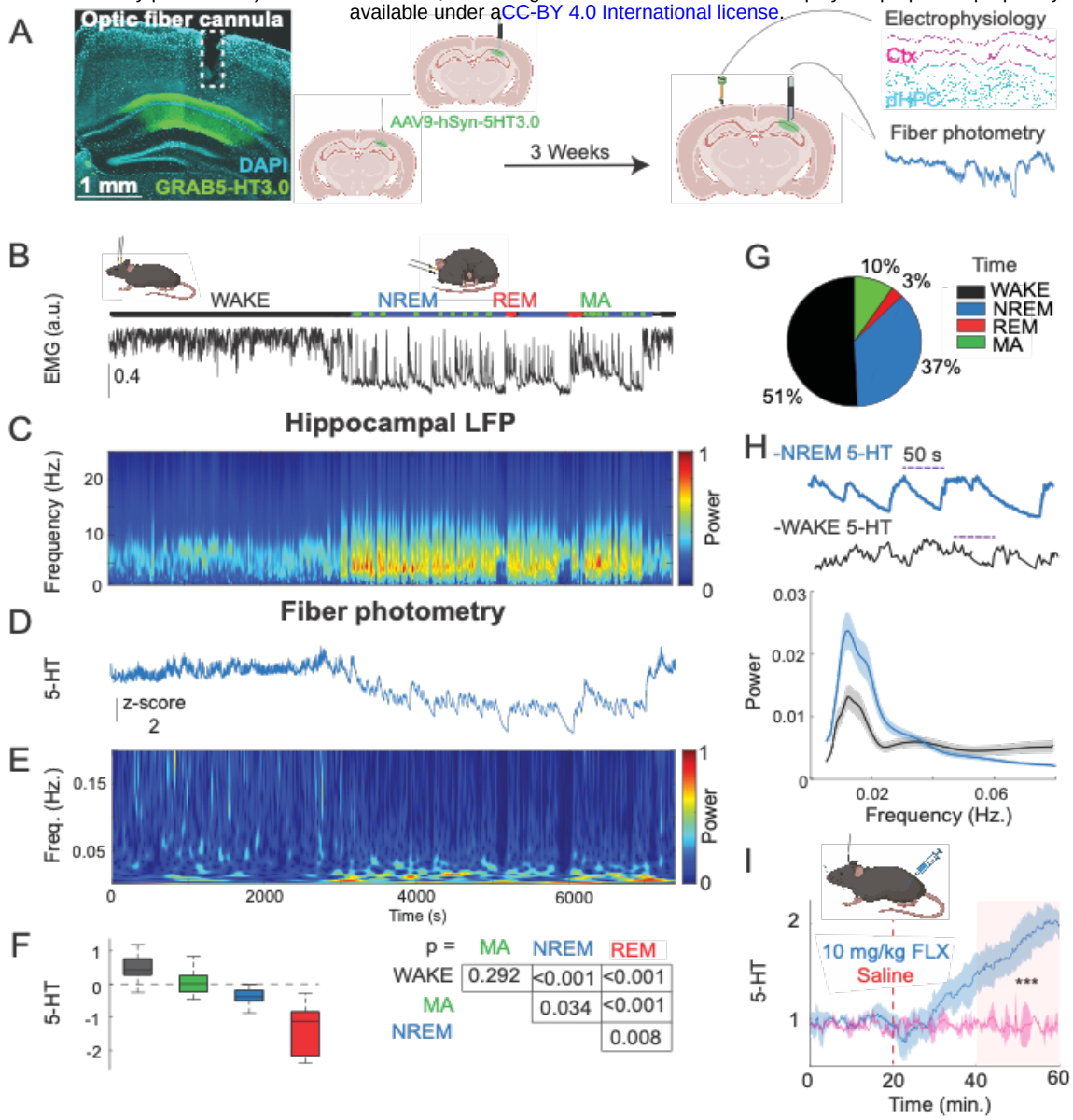

Figure 1. 5-HT levels exhibit ultraslow oscillations during NREM and WAKE.

A. Histology and experimental protocol. Left: expression of GRAB5-HT3.0 sensor (in green) in dorsal CA1 with optic fiber track above. Right: methodology for dual implantation surgeries. AAV9-hSyn-5HT3.0 was first injected into the right dorsal CA1. In the same surgery, an optic fiber was implanted above the injection site. After three weeks of viral expression, a silicon probe was implanted above the left dorsal CA1. Simultaneous recording of the GRAB5-HT3.0 sensor activity (fiber photometry) and electrophysiology was performed. **B-E.** Example dual fiber photometry-electrophysiology recording with times shown in **E**. **B.** Labeled sleep states resulting from automated sleep-scoring and intracranial EMG trace. **C.** Spectrogram (Stockwell transform) showing normalized power of a hippocampal LFP channel during awake and sleep states. **D.** Z-scored 5-HT trace. **E.** Spectrogram (Stockwell transform) of the 5-HT trace shown in **D**. **F.** Left: Mean 5-HT level by state, across all experiments (total n=6 mice, 12 recording sessions of 1.5-3 hours). Right: p-values from a multiple comparisons test applied after fitting a Bayesian linear mixed effects model to the data. **G.** Pie chart showing proportion of time spent in different behavioral states, averaged across all experiments. **H.** Top: examples of ultraslow 5-HT oscillations in NREM and WAKE. Bottom: Power spectrum of 5-HT signals in WAKE vs. NREM sleep. **I.** Control fluoxetine and saline injection experiments. A significant difference between the post-injection period of saline-injected and fluoxetine-injected animals (shaded in red) was observed (Wilcoxon ranked-sum test, $p<0.001$, n= 3 mice).

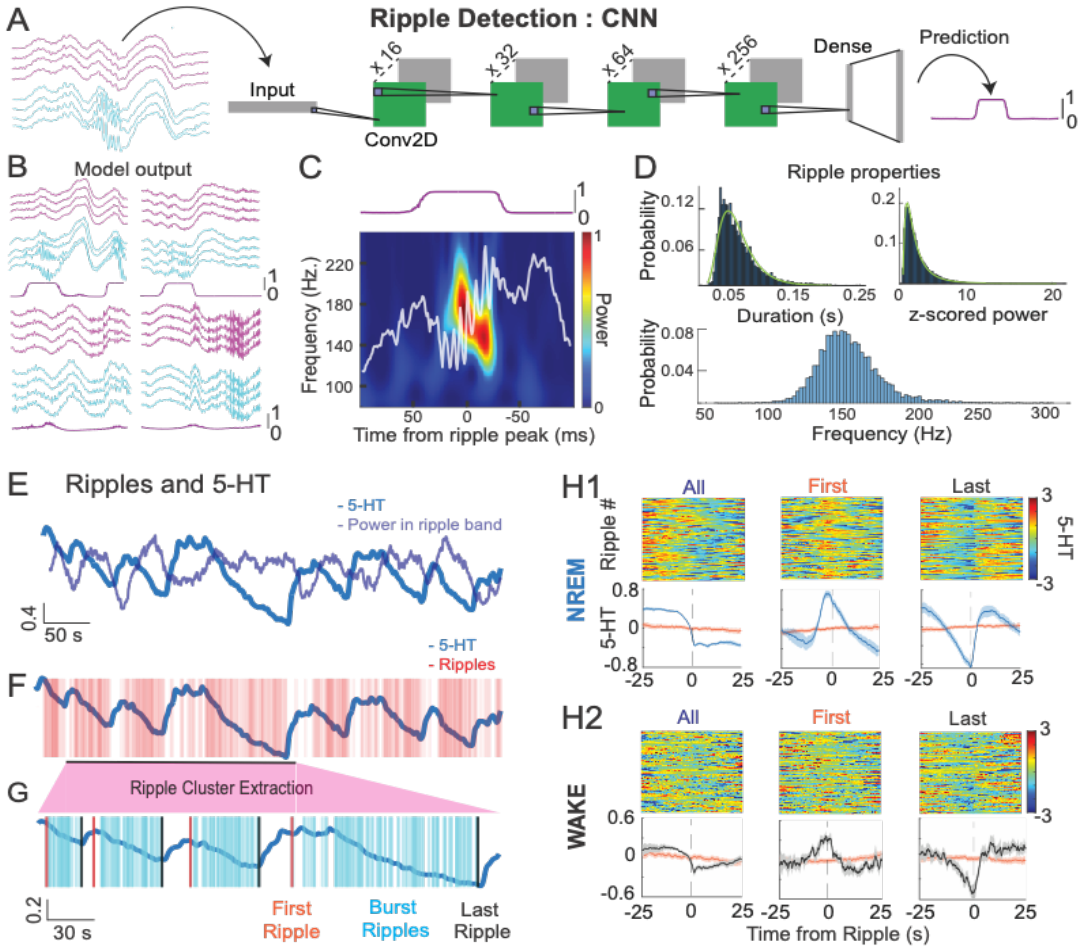

Figure 2. Ripples occur time-locked to ultraslow 5-HT oscillations.

A. Schematic showing the convolutional neural network used for ripple detection. 8-channel x 400 ms-LFP chunks were used as input. The bottom four channels (cyan) were taken from the dorsal CA1 and contained ripples, and the top four channels (magenta) were chosen from a non-adjacent part of the neocortex above the dorsal CA1. The model consisted of four convolution blocks ('Conv2d'), each block comprising a 2D convolutional layer, a ReLU activation function, and batch normalization. Two dense layers with dropout and batch normalization ('Dense') followed and produced the final output, a 400 ms vector with values between 0-1, indicating the probability of a ripple occurring during the course of the input chunk. **B.** Example model output given the four LFP chunk inputs shown. First row: true positives. Second row: fast oscillations and movement artifacts not detected as ripples by the model. **C.** Spectrogram from a ripple detected by the model, 0-1 normalized. **D.** Characteristics of detected ripples. Ripples from all experiments were included, and probability distributions are shown. Top left: distribution of duration. Top right: distribution of z-score normalized ripple power. Bottom: distribution of ripple frequency. Ripple duration and normalized ripple power follow a log-normal distribution (duration: X^2 (df = 7, N = 49,458) = 1.398e+03, p < .0001, normalized ripple power: X^2 (df = 7, N = 49,458) = 422.1862, p < .0001). **E.** Example 5-HT trace and computed power in the ripple band (120-250 Hz). **F.** Same example 5-HT trace and individual detected ripples. **G.** Example of ripple cluster extraction. Ripple clusters were defined as having a minimum of 10 ripple events and an inter-ripple interval of less than 3 seconds. Note the few ripples occurring during the rising phase of 5-HT ultraslow oscillations in **F** are excluded from extracted ripple clusters in **G**. From

these ripple clusters, the first (orange) and last (black) ripples in a cluster were extracted. **H1-2.** Ripple-triggered 5-HT in NREM (**H1)** and WAKE (**H2**) states. The first rows of **H1** and **H2** show all 50 s 5-HT segments centered around the ripple peak for different combinations of ripples (columns). In the first column, all ripples in the given state were included. The second and third columns used only the first or last ripple in extracted ripple clusters, respectively. The second rows of **H1** and **H2**. show the mean ripple-triggered 5-HT traces (blue) and randomly shifted traces (orange) for each group of ripples. The orange traces were obtained by randomly shifting the ripple times for each condition and averaging the resulting 5-HT 50 s segments centered around those shifted times.

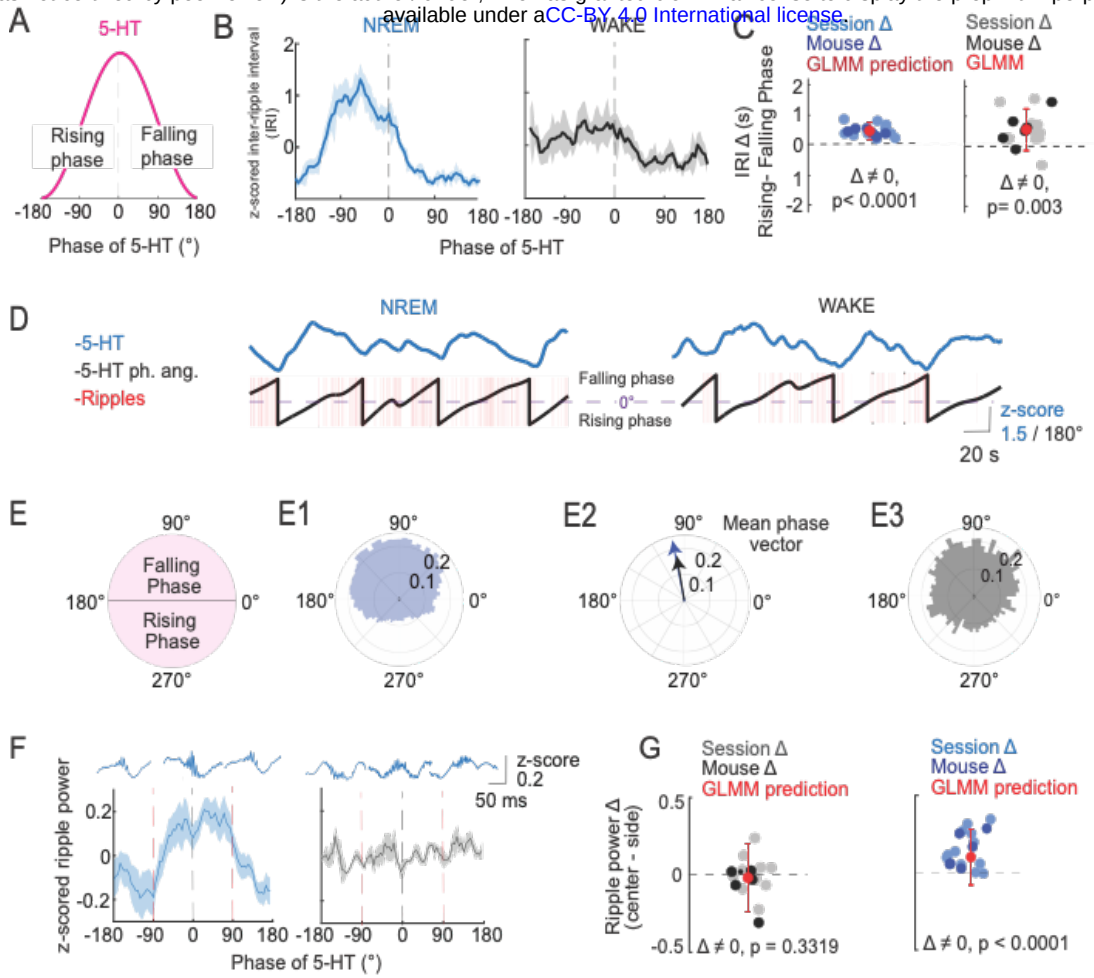

Figure 3. Ripples occurrence and power vary by the phase of ultraslow 5-HT oscillations.

A. Schematic showing one period of a slow 5-HT oscillation. The rising phase of the oscillation occurs from -180° to 0°, and the falling phase occurs from 0° to 180°. **B.** Mean z-scored inter-ripple interval (IRI) by 5-HT phase angle during NREM (left) and WAKE (right). **C.** Mean rising phase IRI - mean falling phase IRI, plotted by session and mouse level in WAKE (left) and NREM (right). Red point with error bar indicates predicted difference and confidence interval after fitting a general linear mixed effects model to the data. P-values shown were derived from a post-hoc multiple comparisons test on the fitted model. (n=6 mice, 12 sessions). **D.** Example 5-HT trace (top) and corresponding 5-HT phase angles and ripples (bottom) for NREM (left) and sleep (right). The peak of the slow oscillation (0°) is indicated by the dashed purple line. **E1. S**chematic polar plot showing one period for a slow 5-HT oscillation. The falling phase of the oscillation occurs from 0° to 180°, and the rising phase occurs from 180° to 0°. **E2.** Phase of all NREM ripples relative to the ultraslow 5-HT oscillation. **E4.** Phase of all WAKE ripples relative to the ultraslow 5-HT oscillation. **E3.** Mean phase vector of NREM and WAKE ripples. **F.** Z-scored ripple power by 5-HT phase angle during NREM (left) and WAKE (right). Red vertical dashed lines delineate analyzed phase segments: 'center '(-90° to 90°) vs. 'side '(-180° to -90° and 90° to 180°). Representative ripples from each phase grouping are shown above. **G.** Mean center phase ripple power - mean side phase ripple power, plotted by session and mouse level in WAKE (left) and NREM (right). Red point with error bar indicates predicted difference and confidence interval after fitting a general linear mixed effects model to the data. P-values shown were derived from a post-hoc multiple comparisons test on the fitted model.

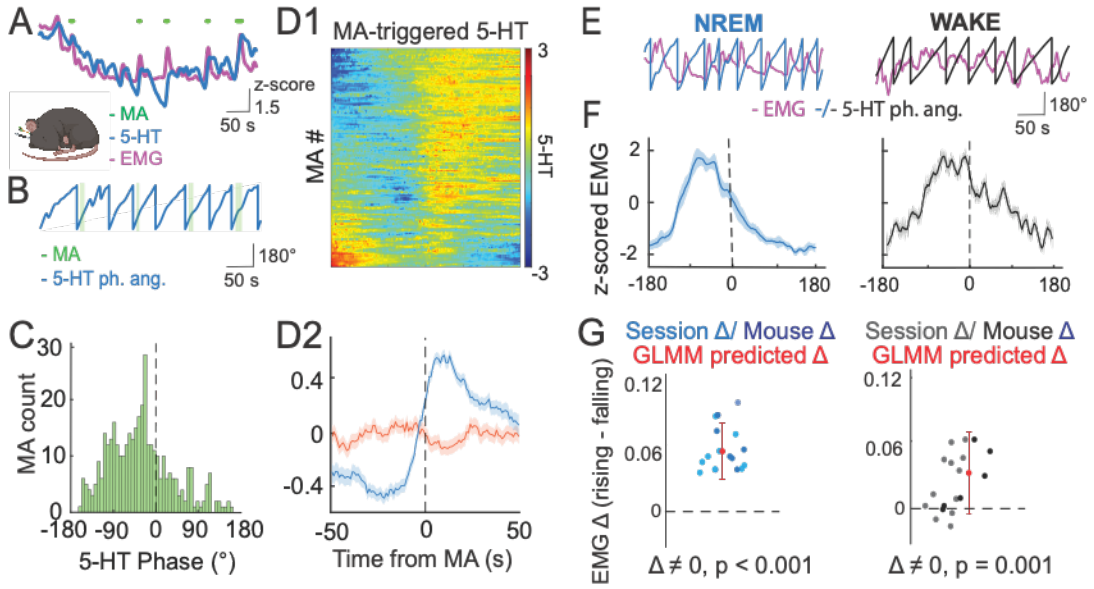

Figure 4. EMG and MAs vary by the phase of ultraslow 5-HT oscillations.

A.-D2. Relationship between microarousal (MA) occurrence and the phase of slow 5-HT oscillations. **A.** Example trace showing 5-HT, EMG, and MAs during a NREM bout. **B.** Example trace showing extracted 5-HT phase angle and MAs. **C**. MA occurrence according to 5-HT phase angle. **D1.** MA-triggered 5-HT across all MA events. **D2.** Mean MA-triggered 5-HT trace (blue) plotted with mean of randomly shifted 5-HT trace (orange). The orange trace was derived by randomly shifting all MA times and averaging the resulting 5-HT segments around those shifted times. **E.-G.** Relationship between the EMG signal and phase of slow 5-HT oscillations. **E.** Example traces showing extracted 5-HT phase angle and the EMG signal during NREM (left, blue) and WAKE (right, black) states. **F.** Mean z-scored EMG signal by 5-HT phase angle during NREM and WAKE states. **G.** Mean rising phase EMG - mean falling phase EMG, plotted by session and mouse level. Red point with error bar indicates predicted difference and confidence interval after fitting a general linear mixed effects model to the data. P-values shown were derived from a post-hoc multiple comparisons test on the fitted model.

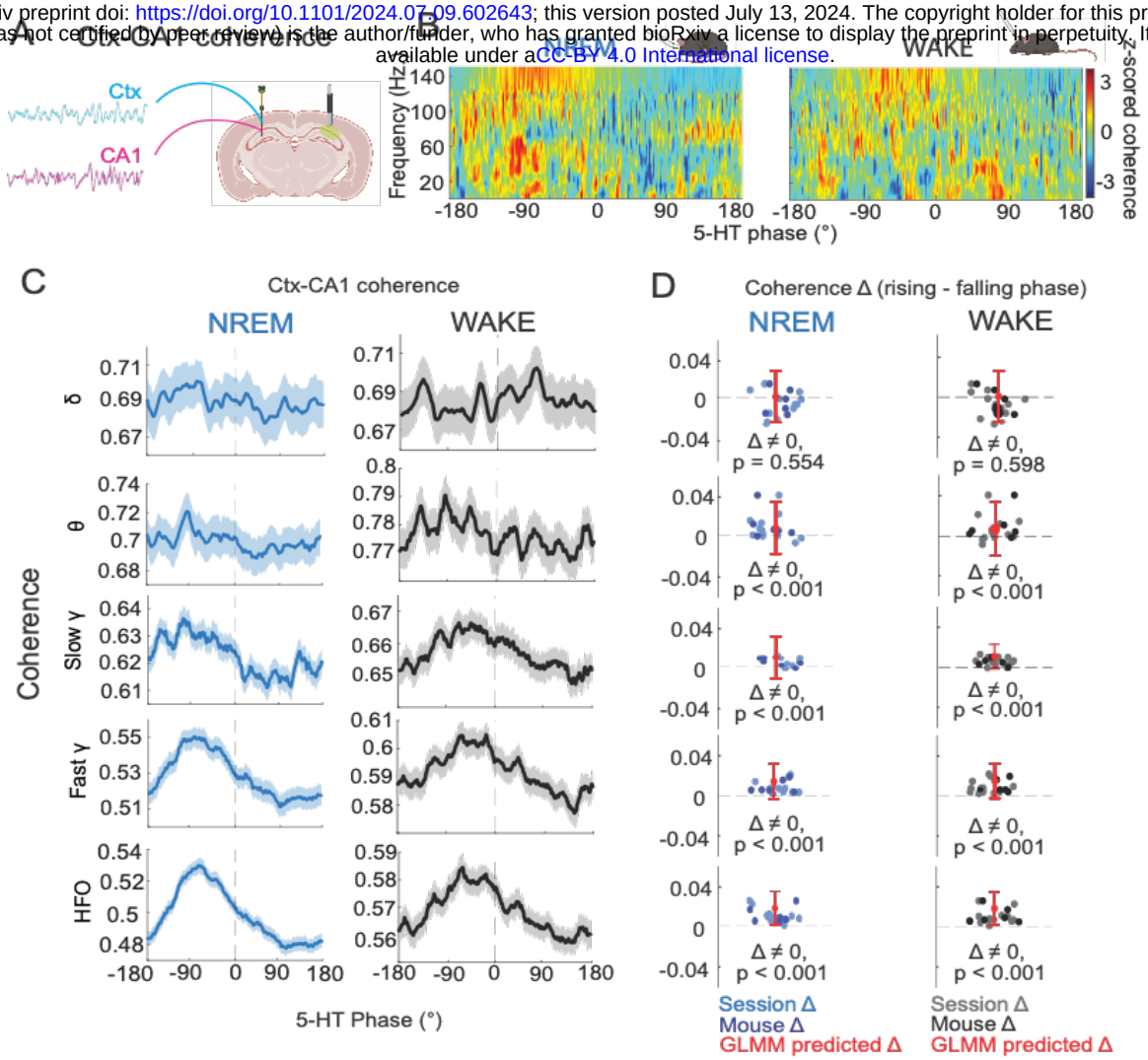

Figure 5. Coherence varies by the phase of ultraslow 5-HT oscillations

A. Schematic showing representative hippocampal and cortical traces used for coherence calculations. **B.** Mean z-scored hippocampal-cortical coherence by frequency for NREM (left) and WAKE (right). **C.** Mean coherence by 5-HT phase angle for delta (1-5 Hz.), theta (6-10 Hz.), slow gamma (30-60 Hz.), fast gamma (60-100Hz.) and high frequency oscillation (HFO, 100-150 Hz.) bands in NREM (left column) and WAKE (right column). **D.** Mean rising phase coherence - mean falling phase coherence, plotted by session and mouse level for different frequency bands (rows) and states (columns). Red point with error bar indicates predicted difference and confidence interval after fitting a general linear mixed effects model to the data. P-values shown were derived from a post-hoc multiple comparisons test on the fitted model.

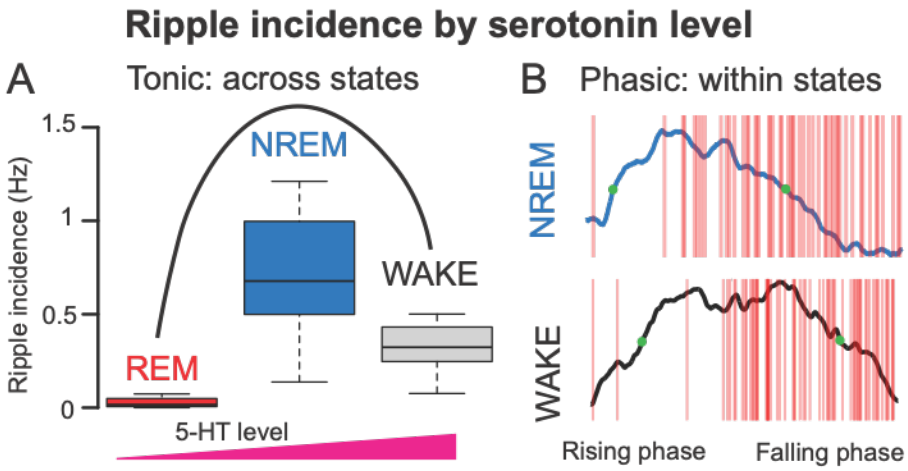

Figure 6. Relationship between ripple incidence and 5-HT levels depends on time-scale

A. Ripple incidence by behavioral state shows an inverted-U dose response relationship, with a peak at intermediate 5-HT levels (see Figure 1F). **B**. Within states, ripple incidence depends on the phase of the ultraslow 5-HT oscillation. At the same absolute 5-HT level (e.g. green dots), therefore, different ripple incidences are observed.